

In this modified approach, the implementation of one-qubit gates is unchanged, but the CNOT implementation must satisfy additional constraints—the action of the exchanges on both the  $S = 1$  and the  $S = 0$  six-spin subspaces must be considered. As a consequence, implementation of CNOT in serial operation is considerably more complex; our numerical studies have failed to identify an implementation (even a good approximate one) for sequences of up to 36 exchanges (compare with 19 in Fig. 2c). On the other hand, we have found implementations using 8 clock cycles for 1D and 2D parallel operation (again for the 1D case  $H_{12}$  can be zero), so use of this larger Hilbert space may well be advantageous in some circumstances.

Finally, we note that further work is needed on the performance of quantum error correction within this scheme. Our logical qubits could be used directly within the error correction codes that have been shown to produce fault-tolerant quantum computation<sup>20</sup>. Spin decoherence would primarily result in ‘leakage’ errors, which would take our logical qubits into states of different angular momentum (for example,  $S = 3/2$ ). Our preliminary work indicates that, with small modifications, the conventional error correction circuits will not cause uncontrolled propagation of leakage error. In addition, the general theory<sup>8,10,20,21</sup> shows that there exist sequences of exchange interactions that directly correct for leakage by swapping a fresh  $|0_I\rangle$  into the coded qubit if leakage has occurred, and doing nothing otherwise; we have not yet identified numerically such a sequence. If fast measurements are possible, teleportation schemes could also be used in leakage correction.

The present results offer an alternative route to the implementation of quantum computation. The trade-offs are clear: for the price of a factor of three more devices, and about a factor of ten more clock cycles, the need for stringent control of magnetic fields applied to individual spins is dispensed with. We hope that the flexibility offered by these results will make easier the hard path to the implementation of quantum computation in the laboratory. □

Received 30 May; accepted 2 October 2000.

- DiVincenzo, D. P. The physical implementation of quantum computation. *Fortsch. Phys.* (special issue: Experimental Proposals for Quantum Computation) (in the press); also as preprint quant-ph/0002077 at (<http://xxx.lanl.gov>) (2000).
- Loss, D. & DiVincenzo, D. P. Quantum computation with quantum dots. *Phys. Rev. A* **57**, 120–126 (1998).
- Kane, B. E. A silicon-based nuclear-spin quantum computer. *Nature* **393**, 133–137 (1998).
- Vrijen, R. *et al.* Electron-spin-resonance transistors for quantum computing in silicon-germanium heterostructures. *Phys. Rev. A* **62**, 012306-1 to 012306-10 (2000).
- Burkard, G., Loss, D. & DiVincenzo, D. P. Coupled quantum dots as quantum gates. *Phys. Rev. B* **59**, 2070–2078 (1999).
- Barenco, A. *et al.* Elementary gates for quantum computation. *Phys. Rev. A* **52**, 3457–3467 (1995).
- DiVincenzo, D. P. *et al.* Quantum computation and spin electronics. In *Quantum Mesoscopic Phenomena and Mesoscopic Devices in Microelectronics* (eds Kulik, I. O. & Ellialtioglu, R.) (NATO ASI, in the press), also as preprint cond-mat/9911245 at (<http://xxx.lanl.gov>) (2000).
- Bacon, D., Kempe, J., Lidar, D. A. & Whaley, K. B. Universal fault-tolerant computation on decoherence-free subspaces. *Phys. Rev. Lett.* **85**, 1758–1761 (2000).
- Viola, L., Knill, E. & Lloyd, S. Dynamical generation of noiseless quantum subsystems. *Phys. Rev. Lett.* **85**, 3520–3523 (2000).
- Kempe, J., Bacon, D., Lidar, D. A. & Whaley, K. B. Theory of decoherence-free fault-tolerant universal quantum computation. *Phys. Rev. A* (submitted); also as preprint quant-ph/0004064 at (<http://xxx.lanl.gov>) (2000).
- Zurek, W. H. Environment-induced superselection rules. *Phys. Rev. D* **26**, 1862–1880 (1982).
- Palma, G. M., Suominen, K.-A. & Ekert, A. K. Quantum computers and dissipation. *Proc. R. Soc. Lond. A* **452**, 567–584 (1996).
- Duan, L.-M. & Guo, G.-C. Reducing decoherence in quantum-computer memory with all quantum bits coupling to the same environment. *Phys. Rev. A* **57**, 737–741 (1998).
- Lidar, D. A., Chuang, I. L. & Whaley, K. B. Decoherence-free subspaces for quantum computation. *Phys. Rev. Lett.* **81**, 2594–2597 (1998).
- Zanardi, P. & Rasetti, M. Error avoiding quantum codes. *Mod. Phys. Lett. B* **11**, 1085–1093 (1997).
- Knill, E. & Laflamme, R. & Viola, L. Theory of quantum error correction for general noise. *Phys. Rev. Lett.* **84**, 2525–2528 (2000).
- Kitaev, A. Y. Quantum computations: algorithms and error correction. *Russ. Math. Surv.* **52**, 1191–1249 (1997).
- Nielsen, M. A. & Chuang, I. L. *Quantum Computation and Quantum Information* Appendix 3 (Cambridge Univ. Press, Cambridge, 2000).
- Makhlin, Y. Nonlocal properties of two-qubits gates and mixed states and optimization of quantum computations. Preprint quant-ph/0002045 at (<http://xxx.lanl.gov>) (2000).
- Preskill, J. in *Introduction to Quantum Computation and Information* (eds Lo, H.-K., Popescu, S. & Spiller, T.) 213–269 (World Scientific, Singapore, 1998).

21. Lidar, D. A., Bacon, D. & Whaley, K. B. Concatenating decoherence-free subspaces with quantum error correcting codes. *Phys. Rev. Lett.* **82**, 4556–4559 (1999).

## Acknowledgements

We thank P. O. Boykin and B. M. Terhal for discussions. D.P.D., D.B., J.K. and K.B.W. were supported by the National Security Agency and the Advanced Research and Development Activity. D.P.D. also thanks the UCLA DARPA program on spin-resonance transistors for support, and is also grateful for the hospitality of D. Loss at the University of Basel, where much of this work was completed. J.K. also acknowledges support from the US National Science Foundation. G.B. is supported in part by the Swiss National Science Foundation.

Correspondence and requests for materials should be addressed to D.P.D. (e-mail: divince@watson.ibm.com).

## Kondo physics in carbon nanotubes

Jesper Nygård\*, David Henry Cobden† & Poul Erik Lindelof\*

\* Ørsted Laboratory, Niels Bohr Institute, Universitetsparken 5, DK-2100 Copenhagen, Denmark

† Department of Physics, University of Warwick, Coventry CV4 7AL, UK

The connection of electrical leads to wire-like molecules is a logical step in the development of molecular electronics, but also allows studies of fundamental physics. For example, metallic carbon nanotubes<sup>1</sup> are quantum wires that have been found to act as one-dimensional quantum dots<sup>2,3</sup>, Luttinger liquids<sup>4,5</sup>, proximity-induced superconductors<sup>6,7</sup> and ballistic<sup>8</sup> and diffusive<sup>9</sup> one-dimensional metals. Here we report that electrically contacted single-walled carbon nanotubes can serve as powerful probes of Kondo physics, demonstrating the universality of the Kondo effect. Arising in the prototypical case from the interaction between a localized impurity magnetic moment and delocalized electrons in a metallic host, the Kondo effect has been used to explain<sup>10</sup> enhanced low-temperature scattering from magnetic impurities in metals, and also occurs in transport through semiconductor quantum dots<sup>11–18</sup>. The far greater tunability of dots (in our case, nanotubes) compared with atomic impurities renders new classes of Kondo-like effects<sup>19,20</sup> accessible. Our nanotube devices differ from previous systems in which Kondo effects have been observed, in that they are one-dimensional quantum dots with three-dimensional metal (gold) reservoirs. This allows us to observe Kondo resonances for very large electron numbers ( $N$ ) in the dot, and approaching the unitary limit (where the transmission reaches its maximum possible value). Moreover, we detect a previously unobserved Kondo effect, occurring for even values of  $N$  in a magnetic field.

Each of our devices<sup>21</sup> contains a metallic single-walled nanotube with gold source and drain contacts and a substrate gate contact, as shown in Fig. 1a. Several measures are taken to optimize electrical contact between the gold and the nanotubes (see Methods). The resulting two-terminal linear-response conductance  $G$  ranges up to more than  $3e^2/h$  (resistance  $8k\Omega$ ) at room temperature, where  $h$  is Planck's constant and  $e$  is the electronic charge. We believe this is the highest reported yet for a single-walled tube<sup>22</sup>. This implies that the transmission probability  $P$  of each contact can reach about 0.9 (the maximum theoretical conductance of a metallic tube is  $1^2 4e^2/h$ ), demonstrating that nearly ideal contacts are achievable between a normal metal and a molecule. Meanwhile, the variation of  $P$  from device to device allows the investigation of different transport regimes.

For  $P \ll 1$ , as is well established<sup>2,3</sup>, Coulomb blockade occurs at low temperature  $T$  and the device behaves as a one-dimensional (1D) quantum dot<sup>23</sup>. The values of the charging energy,  $U$  (the average interaction between two electrons), and the average level spacing,  $\Delta E$ , found for this type of device are as expected for a tube

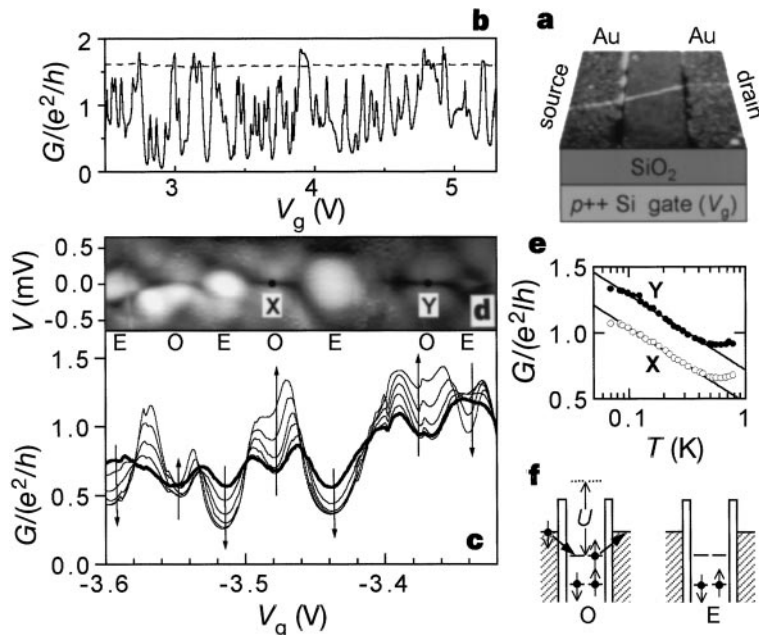


**Figure 1** Characteristics of a nanotube device with intermediate contact transmission probabilities. **a**, Device consisting of a 2-nm-thick nanotube bundle with 30-nm-thick gold contacts separated by 300 nm. Sketched beneath the tapping-mode atomic force microscope (AFM) image are the 300-nm-thick SiO<sub>2</sub> layer and the highly *p*-doped Si substrate used as the gate electrode. **b**, At room temperature (dashed line) the linear-response conductance *G* is about 1.6 *e*<sup>2</sup>/*h*, almost independent of gate voltage *V*<sub>g</sub>. At *T* ≈ 75 mK, the base electron temperature on our dilution refrigerator, reproducible fluctuations are seen in *G* versus *V*<sub>g</sub>. (The source-drain bias *V* used was 7 μV d.c.).

**c**, Temperature dependence of a narrower region of *V*<sub>g</sub>. *T* = 75, 125, 180, 245, 320, 490, 560 and (thicker line) 780 mK. Vertical arrows indicate the direction of change with decreasing *T*, which is opposite in the regions labelled E and O. **d**, Greyscale plot of *dI/dV* against *V* and *V*<sub>g</sub>, over the same region of *V*<sub>g</sub> (darker is more positive). **e**, Conductance versus temperature at points X and Y in **d**. The straight lines indicate log(*T*) behaviour. **f**, Interpretation of the situation in the O and E regions. In O regions the number of electrons *N* on the dot is odd, and higher-order spin-flipping processes can occur, leading to a Kondo resonance. In the E regions *N* is even and no such processes exist.

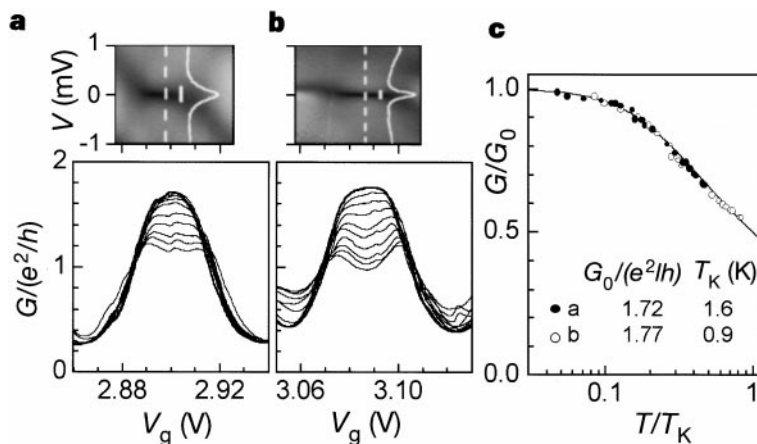


**Figure 2** Analysis of two high-conductance peak pairs. **a**, **b**, Temperature dependence of *G* versus *V*<sub>g</sub>. *T* = 75 (thick line), 87, 150, 200, 250, 330, 420, 530, 630 and 740 mK. Above are *dI/dV* greyscales at 75 mK in the same regions of *V*<sub>g</sub>, showing broad Kondo ridges. Superimposed on each is the *dI/dV* versus *V* trace along the dashed line, which

also serves to denote *dI/dV* = 0. The vertical white bars are of length 2*k*<sub>B</sub>*T*<sub>K</sub>/*e*, where *T*<sub>K</sub> is obtained in each case from the data in **c**. **c**, *G* versus *T* data in the valley centres for the peak pairs in **a** and **b**, scaled in each case to match the theoretical scaling function given in the text (solid line). The deduced values of *G*<sub>0</sub> and *T*<sub>K</sub> are given.

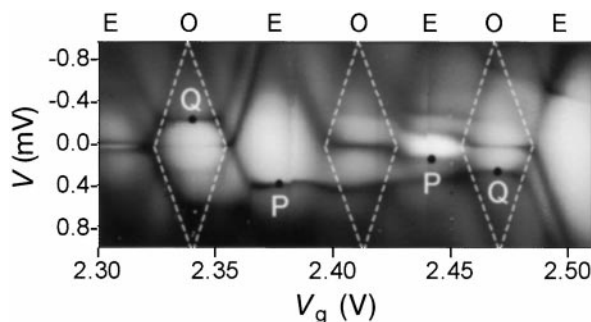


**Figure 3** *dI/dV* greyscale plot in a different *V*<sub>g</sub> region at *T* = 75 mK. Dashed lines outline the odd Coulomb diamonds. Horizontal features such as those labelled P and Q suggest

higher-order processes like the second-order one sketched on the right, where tunnelling involves two levels separated by an energy Δ and occurs only for bias *V* ≥ Δ/*e*.

segment of effective length  $L$  equal to the contact spacing<sup>3</sup>. At higher  $T$ , the device exhibits a power-law variation of  $G$  with  $T$ , which is well explained by Luttinger-liquid behaviour<sup>4</sup>. At the other extreme, for  $P \approx 0.9$ , we see no Coulomb blockade, and instead the characteristics<sup>21</sup> resemble those of a diffusive 1D wire even for  $T < 1$  K.

It is the intermediate transmission regime that we focus on here. The measurements in Fig. 1 were made on a device having  $G \approx 1.6 e^2/h$  (we estimate  $P \approx 0.6$ ) at room temperature. At low  $T$ ,  $G$  undergoes large, reproducible fluctuations as a function of substrate gate voltage  $V_g$  (Fig. 1b). Figure 1c shows the variation with  $T$  over a narrower range of  $V_g$ . At  $T = 780$  mK, the fluctuations are regular and can be identified as Coulomb blockade oscillations. However, unlike normal Coulomb blockade, as  $T$  is decreased  $G$  decreases in some valleys, marked above with an E, while it increases in other valleys, marked with an O. Figure 1d shows a greyscale plot of the differential conductance  $dI/dV$  versus source-drain bias  $V$  and  $V_g$  at  $T \approx 75$  mK. The enhanced conductance in the O valleys corresponds to the dark (high  $dI/dV$ ) horizontal features at  $V = 0$ , such as those labelled X and Y. No such lines are seen in the E valleys, which are instead bounded by roughly hexagonal bubbles. Although the distinctness of these features varies with  $V_g$ , O-type and E-type valleys can be seen to alternate for as many as ten consecutive peaks.

These features can be explained by invoking the Kondo effect<sup>11–13</sup>. When the number  $N$  of electrons on the dot is odd, the total spin  $S$  is a half-integer, and second-order processes such as that shown on the left of Fig. 1f can occur. Similar processes, which change the total

spin of the dot, add up coherently to form a correlated many-electron state in which electrons in the two leads are strongly coupled, allowing current flow even under blockade conditions if  $T < T_K$ , the Kondo temperature. When  $N$  is even, however, there is no equivalent process, and thus no current, if  $S = 0$ . This matches the data if in the O valleys  $N$  is odd and  $S = \frac{1}{2}$  while in the E valleys  $N$  is even and  $S = 0$ . Further evidence confirming that features X and Y in Fig. 1d are “Kondo ridges” is provided by the logarithmic dependence<sup>16</sup> of  $G$  on  $T$  in the centres of the ridges, shown in Fig. 1e, and by the splitting of the ridges in a magnetic field (see later).

This new Kondo system differs in several important ways from the two dimensional (2D) semiconductor dots in which Kondo physics was previously studied<sup>14–19</sup>. First, for semiconductor dots the leads are 2D electron systems, while for tube dots they are normal three-dimensional (3D) metal (gold). Second, the excitation spectrum of an interacting 1D dot, which behaves as a Luttinger liquid when Coulomb blockade is overcome<sup>4</sup>, is profoundly different from that of a 2D dot. Third, because semiconductor dots are electrostatically defined, their geometry and contact transmission probabilities depend on gate voltages. In contrast, for tube dots the contacts cannot be individually tuned, but the fixed geometry means that signs of the Kondo effect can be seen over the entire range of  $V_g$ , encompassing hundreds of Coulomb oscillations. Fourth, the effect of a magnetic field is entirely through spin in single-walled nanotube dots, whereas orbital effects are often dominant in semiconductor dots. Fifth, because of the latter, combined with the absence of spin-orbit coupling, unlike the spin of a semiconductor dot, the spin of a tube dot is well defined and

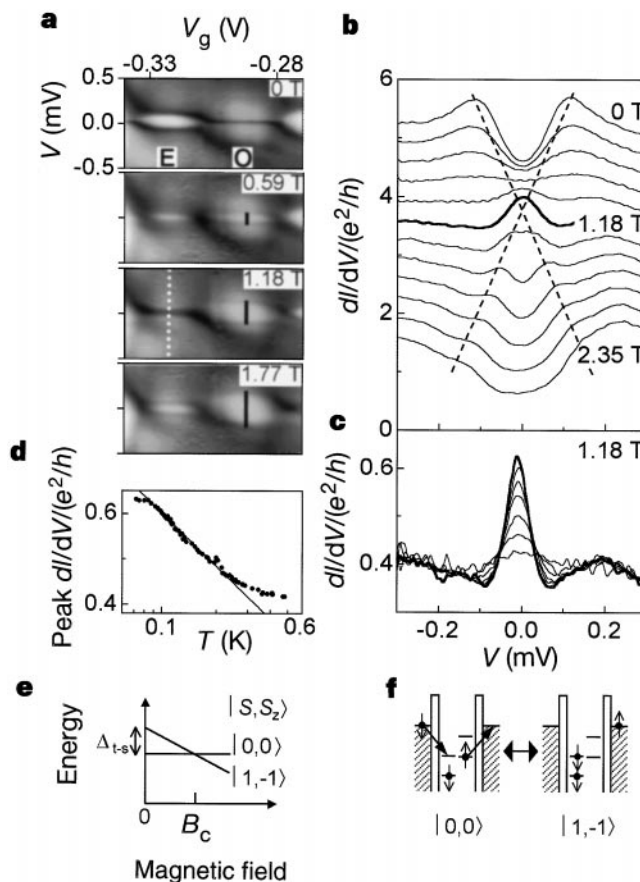


**Figure 4** Effect of perpendicular magnetic field  $B$ . **a**,  $dI/dV$  greyscale plot at  $T = 75$  mK showing adjacent odd- $N$  (O) and even- $N$  (E) regions at a series of fields. The vertical bars have length  $2g\mu_B B/e$ . As  $B$  increases the O ridge splits while the E bubble shrinks to a single ridge at 1.18 T before reappearing at higher  $B$ . **b**, Evolution of  $dI/dV$  versus  $V$  characteristics at  $V_g = -0.322$  V (indicated by the white dotted line in **a**) at  $T = 75$  mK. The traces are offset from each other by  $0.4 e^2/h$  for clarity. The dashed

lines, which indicate the motion of the peaks, are sloped according to  $g\mu_B B/e$ .

**c**, Temperature dependence of the peak in  $dI/dV$  at  $B = 1.18$  T.  $T = 75$  (thick line), 100, 115, 130, 180, 230 and 350 mK. **d**, Peak value of  $dI/dV$  (at  $V = 0$ ) plotted against  $\log(T)$ . **e**, A singlet  $|S, S_z\rangle = |0, 0\rangle$  ground state becomes degenerate with a triplet  $|1, -1\rangle$  excited state at  $B = B_c = \Delta_{t-s}/g\mu_B$ . At this point, spin-flipping higher order transitions, as sketched in **f**, become possible, leading to a new type of Kondo resonance.

easily measured<sup>24,25</sup> even for large  $N$ . Sixth, the conditions<sup>14,23</sup> on the size  $L$  for observing the Kondo effect are weaker in the tube dot. Halfway along a Kondo ridge,  $T_K \approx (\Gamma U)^{1/2} \exp[-(\pi/4)U/\Gamma]$ , where  $\Gamma$  is the level width. The ratio  $U/\Gamma$  cannot be made smaller than  $U/\Delta E$ , because  $\Gamma < \Delta E$  for any quantum dot. For 2D semiconductor dots,  $U/\Delta E \propto L$ , so that the maximum possible  $T_K$  decreases exponentially with  $L$ . This requires them to be made as small as possible, which limits the electron number  $N$  to less than about 100. In contrast, for tube dots, which are 1D,  $U/\Delta E \approx 6$  is independent<sup>3</sup> of length  $L$ , and the maximum  $T_K$  decreases only with the prefactor  $(\Gamma U)^{1/2}$ . This helps to explain how tube dots can show such a strong and clear Kondo effect even for large  $N$ . An order of magnitude estimate of  $N$  is the number of  $\pi$ -electrons in the tube, that is, the number of carbon atoms, which is tens of thousands. (Without knowing the exact dot size or band structure a more accurate estimate is not possible.) Nanotube quantum dots therefore allow the first ever observations, to our knowledge, of the Kondo effect in the limit of very large  $N$ .

The width  $\Gamma$  varies from level to level, so we can search for pairs of peaks with particularly large  $\Gamma$ , such as those shown in Fig. 2a and b. For both of these pairs the valley between the peaks is completely gone at base temperature ( $\sim 75$  mK). In the Kondo regime,  $G$  is expected to saturate at the unitary limit  $G_0$  as  $T \rightarrow 0$ , and at higher  $T$  it should follow a universal scaling form<sup>10</sup> that can be approximated by<sup>15</sup>  $G(T) = G_0/(1 + (2^{1/s} - 1)(T/T_K)^s)^2$ , where  $s = 0.22$  for spin half on the dot. To test this, we fit  $G$  versus  $T$  in the valley centre to this expression, using  $T_K$  and  $G_0$  as fitting parameters. The results, shown in Fig. 2c, are highly satisfactory. For both peak pairs we find  $G_0 > 1.7e^2/h$ , which is close to the maximum value of  $2e^2/h$  obtained for symmetric coupling to the two contacts (this assumes the double Fermi-point degeneracy<sup>1</sup> is broken). The deduced values of  $T_K$  of 1.6 K and 0.9 K are in good agreement with nonlinear measurements, as indicated in the insets above Fig. 2a and b. Here, on top of greyscale plots of  $dI/dV$  showing the Kondo ridges are superimposed traces of  $dI/dV$  versus  $V$  midway along each ridge. The Kondo effect is expected to be suppressed<sup>13</sup> on a bias scale  $|V| \approx k_B T_B/e$ . Indeed, we see that the width of each peak in  $dI/dV$  is roughly  $2k_B T_K/e$  (indicated by the vertical white bars). We believe these measurements on a nanotube dot are closer to the unitary limit than has previously been reported in a semiconductor quantum dot.

In some regions of  $V_g$ , such as that shown in Fig. 3, a regular series of faint diamonds can be discerned. This resembles the standard behaviour of a quantum dot for  $P \ll 1$ , where only first-order tunnelling is significant and Coulomb blockade forces  $N$  to be fixed at an integer within the diamonds. However, superimposed on the diamonds are a variety of horizontal features which can be attributed to higher-order tunnelling processes that are strong in this device because  $P$  is large. Kondo ridges are seen at  $V = 0$  in the odd- $N$  diamonds (marked O again), which are outlined by white dashed lines. Additional horizontal ridges are seen at  $V \neq 0$ , such as those labelled P in the even and Q in the odd diamonds. Features of type P truncate every even diamond, resulting in the characteristic alternating bubble-ridge pattern seen also in Fig. 1d. It is natural to associate a horizontal feature at a bias  $V = \Delta/e$  with processes generating an excitation of energy  $\Delta$  in the dot. An example of such a process is co-tunnelling involving two nondegenerate single-particle states, as sketched on the right of Fig. 3. However, since such inelastic co-tunnelling normally only produces a step in  $dI/dV$  above a threshold, we suggest that these peaks in  $dI/dV$  at finite bias offsets are another manifestation of Kondo physics.

Finally, we look at the effect of magnetic field  $B$ . Figure 4a shows the evolution with  $B$  of an adjacent bubble (E) and Kondo ridge (O). As expected<sup>13</sup>, the Kondo ridge splits linearly into components at  $V = \pm g\mu_B B/e$  (the Zeeman energy), where  $\mu_B$  is the Bohr magneton and  $g = 2.0$  is the electron  $g$ -factor<sup>2,25</sup>. Meanwhile, the edges of the bubble move linearly towards  $V = 0$ . Figure 4b shows the  $dI/dV$

characteristics in the centre of the bubble. At a certain field,  $B_c = 1.18$  T, the bubble collapses to a single ridge, corresponding to a peak in  $dI/dV$  at  $V = 0$ . Its  $T$  dependence is shown in Fig. 4c. The peak height is logarithmic in  $T$  (Fig. 4d), just as for the odd- $N$  Kondo ridge at  $B = 0$ . A similar ridge is formed in most bubbles at a field dependent on the bubble width at  $B = 0$ .

Exactly such behaviour has recently been predicted<sup>20</sup> for quantum dots when  $N$  is even, in the case where the Zeeman energy is sufficiently large. It is assumed that at  $B = 0$  the ground state is a singlet ( $S = 0$ ), and the lowest excited state is a triplet ( $S = 1$ ) at a distance  $\Delta_{t-s}$  above the ground state. In an applied field  $B_c = \Delta_{t-s}/g\mu_B$ , the  $S_z = -1$  member of the triplet becomes degenerate with the singlet (see Fig. 4e). At this point,  $S$  alternates between 1 and 0 as electrons co-tunnel between the contacts (see Fig. 4f), resulting in a new type of Kondo resonance<sup>20</sup> with similar characteristics to the conventional type seen at  $B = 0$ . This theory is particularly appropriate to single-walled nanotubes, where the effects of  $B$  are almost entirely through spin. Applying the model, we deduce for instance that the edges of the E bubble in Fig. 4a are associated with a singlet-triplet excitation of energy  $\Delta_{t-s} = g\mu_B B_c = 137 \mu\text{eV}$ .

We note that this new type of Kondo effect is distinct from the one recently discovered in a semiconductor dot<sup>19</sup>, which occurs when a singlet is aligned with a degenerate triplet by orbital effects in a weak magnetic field. It serves to underline the fact that new physical phenomena can emerge in the study of molecular nanostructures. □

## Methods

In making devices, the as-grown single-walled nanotube material<sup>26</sup> is sonicated in dichloroethane and deposited on the SiO<sub>2</sub> by diluting with isopropyl alcohol before drying. To improve the contacts: the leads are fabricated as soon as possible after tube deposition by low-energy (10 kV) electron-beam lithography; the polymethylmethacrylate resist is over-exposed to avoid residue; the contact metallization is pure gold, evaporated directly on top of the tubes; and each contact covers at least 0.5  $\mu\text{m}$  of the tube or bundle. Although we cannot resolve the difference between a single tube and a thin bundle of tubes in the atomic force microscope, we study only devices whose detailed characteristics imply that the conduction is determined by a single metallic nanotube<sup>21</sup>.

Received 30 May; accepted 3 October 2000.

- Dekker, C. Carbon nanotubes as molecular quantum wires. *Phys. Today* **52**, 22–28 (1999).
- Tans, S. *et al.* Individual single-walled carbon nanotubes as quantum wires. *Nature* **386**, 474–477 (1997).
- Bockrath, M. *et al.* Single-electron transport in ropes of carbon nanotubes. *Science* **275**, 1922–1925 (1997).
- Bockrath, M. *et al.* Luttinger-liquid behaviour in carbon nanotubes. *Nature* **397**, 598–601 (1999).
- Yao, Z., Postma, H. W. C., Balents, L. & Dekker, C. Carbon nanotube intramolecular junctions. *Nature* **402**, 273–276 (1999).
- Kasumov, A. Y. *et al.* Supercurrents through single-walled carbon nanotubes. *Science* **284**, 1508–1511 (1999).
- Morpurgo, A. F., Kong, J., Marcus, C. & Dai, H. Gate-controlled superconducting proximity effect in carbon nanotubes. *Science* **286**, 263–265 (1999).
- Frank, S., Poncharal, S. P., Wang, Z. L. & de Heer, W. A. Carbon nanotube quantum resistors. *Science* **280**, 1744–1746 (1998).
- Bachtold, A. *et al.* Aharonov–Bohm oscillations in carbon nanotubes. *Nature* **397**, 673–675 (1999).
- Hewson, A. C. *The Kondo Problem to Heavy Fermions* (Cambridge Univ. Press, Cambridge, 1993).
- Glazman, L. I. & Raikh, M. E. Resonant Kondo transparency of a barrier with quasilocal impurity states. *JETP Lett.* **47**, 452–455 (1988).
- Ng, T. K. & Lee, P. A. On-site Coulomb repulsion and resonant tunneling. *Phys. Rev. Lett.* **61**, 1768–1771 (1988).
- Meir, Y., Wingreen, N. S. & Lee, P. A. Low-temperature transport through a quantum dot: the Anderson model out of equilibrium. *Phys. Rev. Lett.* **70**, 2601–2604 (1993).
- Goldhaber-Gordon, D. *et al.* Kondo effect in a single-electron transistor. *Nature* **391**, 156–159 (1998).
- Goldhaber-Gordon, D. *et al.* From the Kondo regime to the mixed-valence regime in a single-electron transistor. *Phys. Rev. Lett.* **81**, 5225–5228 (1998).
- Cronenwett, S. M., Oosterkamp, T. H. & Kouwenhoven, L. P. A tuneable Kondo effect in quantum dots. *Science* **281**, 540–544 (1998).
- Schmid, J., Weis, J., Eberl, K. & v. Klitzing, K. A quantum dot in the limit of strong coupling to reservoirs. *Physica B* **256–258**, 182–185 (1998).
- Simmel, F., Blick, R. H., Kotthaus, J. P., Wegscheider, W. & Bichler, M. Anomalous Kondo effect in a quantum dot at nonzero bias. *Phys. Rev. Lett.* **83**, 804–807 (1999).
- Sasaki, S. *et al.* A novel Kondo effect in an integer-spin quantum dot. *Nature* **405**, 764–767 (2000).
- Pustilnik, M., Avishai, Y. & Kikoin, K. Quantum dots with even number of electrons: Kondo effect in a finite magnetic field. *Phys. Rev. Lett.* **84**, 1756–1759 (2000).
- Nygård, J., Cobden, D. H., Bockrath, M., McEuen, P. L. & Lindelof, P. E. Electrical transport measurements on single-walled carbon nanotubes. *Appl. Phys. A* **69**, 297–304 (1999).
- Soh, H. T. *et al.* Integrated nanotube circuits: Controlled growth and ohmic contacting of single-walled carbon nanotubes. *Appl. Phys. Lett.* **75**, 627–629 (1999).

23. Glazman, L. I. Single electron tunneling. *J. Low Temp. Phys.* **118**, 247–269 (2000).  
 24. Tans, S., Devoret, M. H., Groeneveld, R. J. A. & Dekker, C. Electron–electron correlations in carbon nanotubes. *Nature* **394**, 761–764 (1998).  
 25. Cobden, D. H., Bockrath, M., McEuen, P. L., Rinzler, A. G. & Smalley, R. E. Spin splitting and even-odd effects in carbon nanotubes. *Phys. Rev. Lett.* **81**, 681–684 (1998).  
 26. Thess, A. *et al.* Crystalline ropes of metallic carbon nanotubes. *Science* **273**, 483–487 (1996).

**Acknowledgements**

We thank A. Rinzler and R. Smalley for supplying the nanotubes, K. G. Rasmussen, M. M. Andreasen, A. E. Hansen and A. Kristensen for experimental assistance, and M. Pustilnik, N. Wingreen, L. P. Kouwenhoven, N. d’Ambrumenil, P. R. Poulsen and P. L. McEuen for helpful discussions.

Correspondence should be addressed to D.H.C. (e-mail: d.h.cobden@warwick.ac.uk).

**Increased marine production of N<sub>2</sub>O due to intensifying anoxia on the Indian continental shelf**

S. W. A. Naqvi, D. A. Jayakumar\*, P. V. Narvekar, H. Naik, V. V. S. S. Sarma\*, W. D’Souza, S. Joseph & M. D. George

National Institute of Oceanography, Dona Paula, Goa 403 004, India

Eutrophication of surface waters and hypoxia in bottom waters has been increasing in many coastal areas<sup>1–4</sup>, leading to very large depletions of marine life in the affected regions<sup>4</sup>. These areas of high surface productivity and low bottom-water oxygen concentration are caused by increasing runoff of nutrients from land. Although the local ecological and socio-economic effects have received much attention<sup>2–4</sup>, the potential contribution of increasing hypoxia to global-change phenomena is unknown. Here we report the intensification of one of the largest low-oxygen zones in the ocean, which develops naturally over the western Indian continental shelf during late summer and autumn. We also report the highest accumulations yet observed of hydrogen sulphide (H<sub>2</sub>S) and nitrous oxide (N<sub>2</sub>O) in open coastal waters. Increased N<sub>2</sub>O production is probably caused by the addition of anthropogenic nitrate and its subsequent denitrification, which is favoured by hypoxic conditions. We suggest that a global expansion of hypoxic zones may lead to an increase in marine production and emission of N<sub>2</sub>O, which, as a potent greenhouse gas, could contribute significantly to the accumulation of radiatively active trace gases in the atmosphere<sup>5</sup>.

The coastal zone off western India experiences moderate upwelling during June–November<sup>6,7</sup>. However, the cold, saline upwelled water is usually capped by a 5–10-m thick warm, lower-salinity layer arising from large land runoff and local precipitation, causing strong stratification and poor ventilation of sub-pycnocline waters. The upwelled water is derived from a poleward under-current, located just off the shelf break<sup>8</sup>, which has an oxygen (O<sub>2</sub>) content of about 0.5 ml l<sup>-1</sup> (22 μM) at 15° N. Over the shelf, the O<sub>2</sub> content is quickly depleted to near-zero levels owing to excessive consumption fuelled by high primary production mainly within the pycnocline (>500 mg C m<sup>-3</sup> d<sup>-1</sup>)<sup>9</sup>. During September–October 1999, severely hypoxic (O<sub>2</sub> < 22 μM) waters were found over almost the entire shelf (Fig. 1), covering an area of about 180,000 km<sup>2</sup>—an order of magnitude greater than the area

(20,000 km<sup>2</sup>) of the largest human-induced hypoxic zone in the Gulf of Mexico<sup>3</sup>.

Sub-pycnocline O<sub>2</sub> depletion over the western Indian shelf, as in other similar environments off Namibia<sup>10</sup> and Peru<sup>11</sup>, is primarily of natural origin because the nutrient enrichment occurs mainly through upwelling; however, it has not been known to be as severe as observed in the present study. For example, observations in October 1999 along a cross-shelf transect off Bombay revealed the prevalence of reducing conditions over much of the shelf with a progression from hypoxic (nonreducing; NO<sub>2</sub><sup>-</sup> [nitrite] = 0, O<sub>2</sub> > 4.4 μM) to suboxic (denitrifying; NO<sub>3</sub><sup>-</sup>, NO<sub>2</sub><sup>-</sup> > 0, 0 < O<sub>2</sub> < 4.4 μM) and then to anoxic (sulphate reducing; NO<sub>3</sub><sup>-</sup>, NO<sub>2</sub><sup>-</sup>, O<sub>2</sub> = 0) regimes as the upwelled water moved up from the shelf-break to the inner-shelf (Fig. 2). These conditions start developing in June, reach peak intensity by September–October and dissipate by December. Thus, this shallow, seasonal suboxic zone is distinct from the deeper, perennial suboxic layer of the central Arabian Sea<sup>12</sup>.

On three of our five cruises during the upwelling period, H<sub>2</sub>S was frequently detected in concentrations reaching up to 19 μM over the inner-shelf north of about 12° N latitude as well as on numerous occasions along the shorter transect off Goa. Instances of sulphate reduction in open-oceanic waters have been recorded off Peru (often without H<sub>2</sub>S analysis)<sup>11,13</sup>, but never before off India. This is presumably because although the O<sub>2</sub> levels were low, the water was not completely anoxic. The earliest data sets (in the 1950s, refs 6, 7

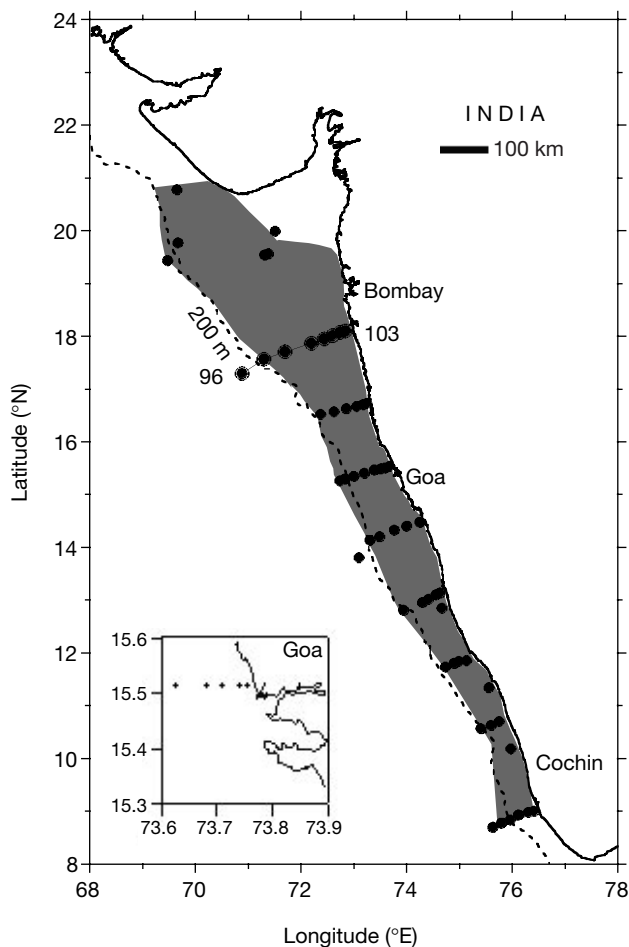


**Figure 1** Zone of severe hypoxia on the western Indian shelf during September–October 1999 and locations of sampling sites. Zone of hypoxia is shown as shaded region (O<sub>2</sub> < 0.5 ml l<sup>-1</sup>). Large circles represent stations occupied during the cruises whereas the five shallow stations (depth 6–28 m) comprising the shorter section off Goa are shown by small circles in the inset.

\* Present addresses: Department of Geosciences, Princeton University, Princeton, New Jersey 08544-1003, USA (D.A.J.); and CEREGE, Université d’Aix-Marseille III, Europole de l’Arbois, BP 80, Cedex 4, 13545 Aix en Provence, France (V.V.S.S.S.).